Blue Economy

Volume 1 | Issue 2 Article 7

2023

Remote Sensing and Radiometric studies of Gabal kadabora – Gabal Umm Ghieg and its surrounding area, Central Eastern Desert, Egypt

Hend Ibrahim Abd-Elmageed
Geology Department, Faculty of Science, Damanhour University, Egypt, hend.ibrahim30@outlook.com

Mohamed Elsadek M. Sabra
Egyptian Mineral Resources Authority, Cairo, Egypt

Tharwat Ahmed Abdel Fattah
Geology Department, Faculty of Science, Alexandria University, Egypt

Elhamy Tarabees
Geology Department, Faculty of Science, Damanhour University, Egypt

Mohamed A.S. Youssef
Nuclear Materials Authority, Cairo, Egypt

ISSN: 2805-2986 – e-ISSN: 2805-2994

Remote Sensing and Radiometric studies of Gabal kadabora – Gabal Umm Ghieg and its surrounding area, Central Eastern Desert, Egypt

Authors

Hend Ibrahim Abd-Elmageed, Mohamed Elsadek M. Sabra, Tharwat Ahmed Abdel Fattah, Elhamy Tarabees, Mohamed A.S. Youssef, and Al Sayeda Abou shagar

RESEARCH ARTICLE

Remote Sensing and Radiometric Studies of Gabal Kadabora − Gabal Umm Ghieg and Its Surrounding Area, Central Eastern Desert, Egypt

Hend I. Abd-Elmageed [a,*], Mohamed E.M. Sabra [b], Tharwat A.A. Fattah [c], Elhamy Tarabees [a], Mohamed A.S. Youssef [d], Al S. Abou shagar [e]

[a] Geology Department, Faculty of Science, Damanhour University, Beheira, Egypt
[b] Egyptian Mineral Resources Authority, Cairo, Egypt
[c] Geology Department, Faculty of Science, Alexandria University, Alexandria, Egypt
[d] Nuclear Materials Authority, Cairo, Egypt
[e] National Institute of Oceanography and Fisheries (NIOF), Egypt

Abstract

Gabal Kadabora − Gabal Umm Gheig and its surrounding area are located in Central Eastern Desert (CED). This region is dominated by igneous, metamorphic, and sedimentary rocks ranging in age from the Late Proterozoic to the Quaternary. Based on the published geological map, Digital elevation model (DEM) and Radiometric map three structural trends: NW−SE, NE−SW, and N−S directions are detected. Spectrometric data vary from 1.86 to 184.58 μR/h for the total count (T.C), from 0.08 to 4.07% for K, from 0.11 to 11.25 ppm for eU, and from 0.4 to 29.33 ppm for eTh. Identification of radiometric anomalies was performed by calculating the factor (X+2σ) for eU, eU/eTh, and eU/K measurements for all single sites in each rock unit. Radiometric analysis indicates the presence of many regions for uranium exploration, where thirteen relatively high uraniferous zones are suggested for further exploration. Correlation between uraniferous zones and lineament distribution shows that some highly uraniferous parts exist where high lineament density prevails. Moreover, some uraniferous parts exist at the boundaries between the rock units.

Keywords: Digital elevation model, Radiometric analysis and uraniferous zones, Structural trends

1. Introduction

The Eastern Desert of Egypt covers about 223 000 km^2, 22% of the Egyptian territory. Integrated geophysical exploration programs proved to be successful in identifying surface evidence of mineralization or associated structures/alteration zones (e.g., Ammar et al., 1983; Mohanty et al., 2011; Chaturvedi et al., 2013; Patra et al., 2013; Gaafar; 2014; Aboelkhair et al., 2020; Diab et al., 2022; Gabr et al., 2022).

This work integrates remote sensing and radiometric methods to define the anomalous zones and structural framework of Gabal Kadabora − Gabal Umm Gheig and its surrounding area, Central Eastern Desert, Egypt. The area under investigation lies at the Central part of the Eastern Desert between longitudes 34° 00′ 43.42″ E and 34° 39′ 37.81″ E and latitudes 25° 10′ 19.77″ N and 25° 30′ 08.65″ N (Fig. 1), covering an area of about 2387.4 km^2. In order to investigate how the three radioelements, eU, eTh, and K% are distributed in the study area, as well as the total radiation count, airborne gamma-ray spectrometric data have been used. The interpretation of the radiometric maps and surface geologic map allows for a good correlation between

Received 30 October 2023; revised 19 November 2023; accepted 19 November 2023.
Available online 30 December 2023

* Corresponding author at: Geology Department, Faculty of Science, Damanhour University, Egypt. Fax: 045-3321501.
E-mail address: hend.ibrahim30@outlook.com (H.I. Abd-Elmageed).

https://doi.org/10.57241/2805-2994.1013

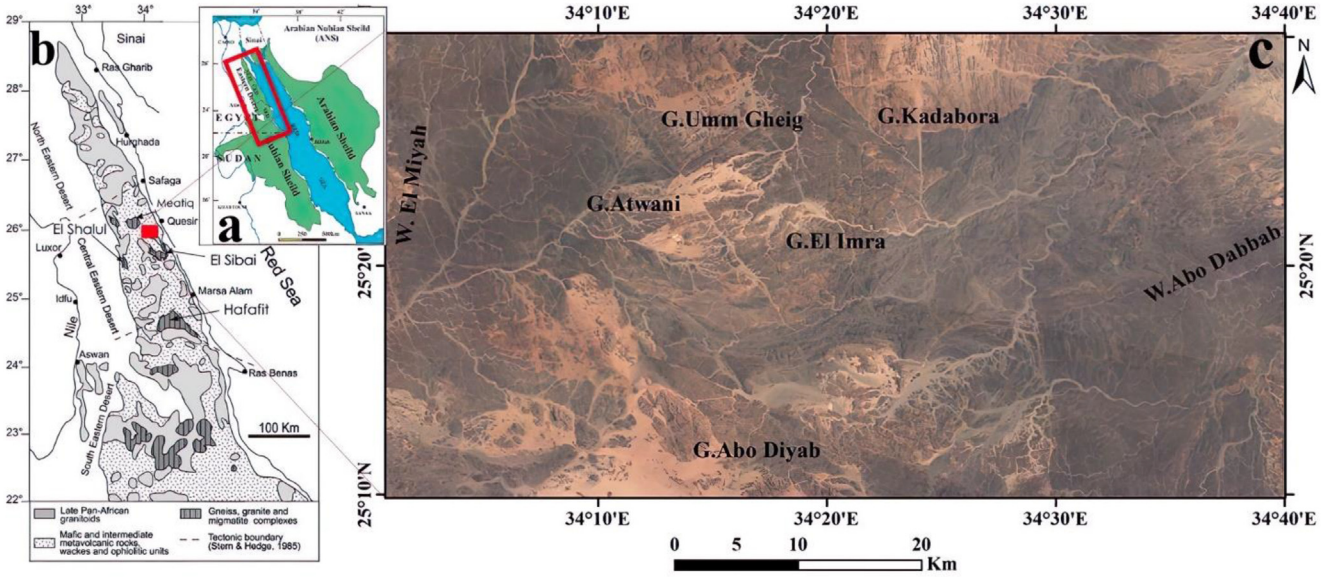

Fig. 1. (a) Location map of the study area, (b) Satellite image showing the study area.

surface and near-surface features. Gamma-ray spectrometric survey is commonly used for mineral prospecting, geological mapping, and environmental research. The main objectives of this study are to 1) identify the surface structural framework, 2) remap the geologic map based on the radioactivity results, and 3) detect uraniferous lead locations.

2. Geologic setting

The Egyptian Eastern Desert has been divided into three domains: Northern Eastern Desert (NED), Central Eastern Desert (CED), and Southern Eastern Desert (SED) (Fig. 1b). This classification reflects the following: 1) higher concentrations of granitic rocks in the NED and SED than in the CED, and 2) the most significant concentrations of rocks with strong oceanic affinities are exposed in the CED. These domains are separated by two ENE–WSW striking fundamental fault zones: the Safaga-Qena zone, which separates the NED from CED domains, and the Marsa Alam-Aswan fault zone, which separates the CED from SED domains (El-Gaby et al., 1988). Fig. 1b shows a satellite map of the study area.

CED is structurally characterized by NNW steeply dipping ductile shear zones and ENE deep-seated faults (El-Ramly, 1972; Garson and Krs, 1976; Stern and Hedge, 1985; Bennett and Mosley, 1987). From the geologic map (Fig. 2), lithostratigraphy of the study area involves A) the Late Proterozoic rocks, comprising a large portion of the region, are posed by the Ophiolite Group, Hammamat clastics, Older Granite, and Younger Granite, B) Cenozoic rocks that include Miocene rocks (Umm Mahara, Ranga Um Gheigh, and Abu Dabbab formations), and then Pliocene Shagara Formation, Quaternary and Wadi

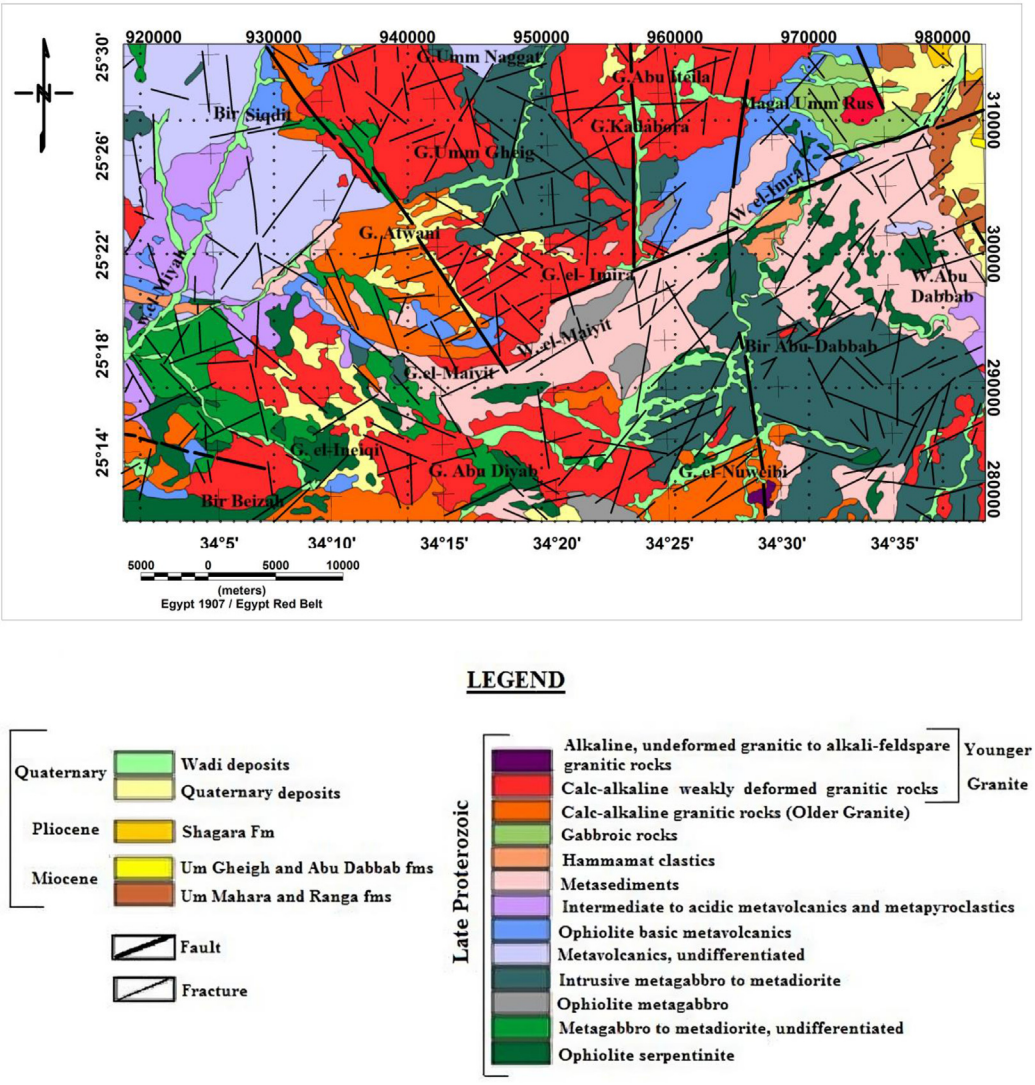

Fig. 2. Geologic map of the study area (After Conoco, 1987).

deposits (Conoco, 1987; EGSMA Egyptian Geological Survey and Mining Authority, 1992; EMRA Egyptian Mineral Resources Authority, 2009). The structural features comprise four main phases of deformations that prevailed during the development of the Eastern Desert as a part of the Arabian–Nubian Shield and the East African Orogeny. These phases are the early compressional phase (D1), the early extensional phase (D2), the late extensional phase (D3), and the late compressional phase (D4) (Bregar et al., 2002; Johnson et al., 2011). The investigated area exhibits three types of fault trends (Fig. 3), which are: 'NE–SW' coincides with the Syrian arc trend, 'NW–SE' coincides with the Red Sea–Gulf of Suez trend, and the 'N–S' coincides with the East African trend (Stern and Hedge, 1985; El-Rakaiby, 1988; Abd El-Wahed, 2008; Hamimi et al., 2015; Sadek et al., 2015; Stern, 2017; El Qassas et al., 2020; Soliman et al., 2021).

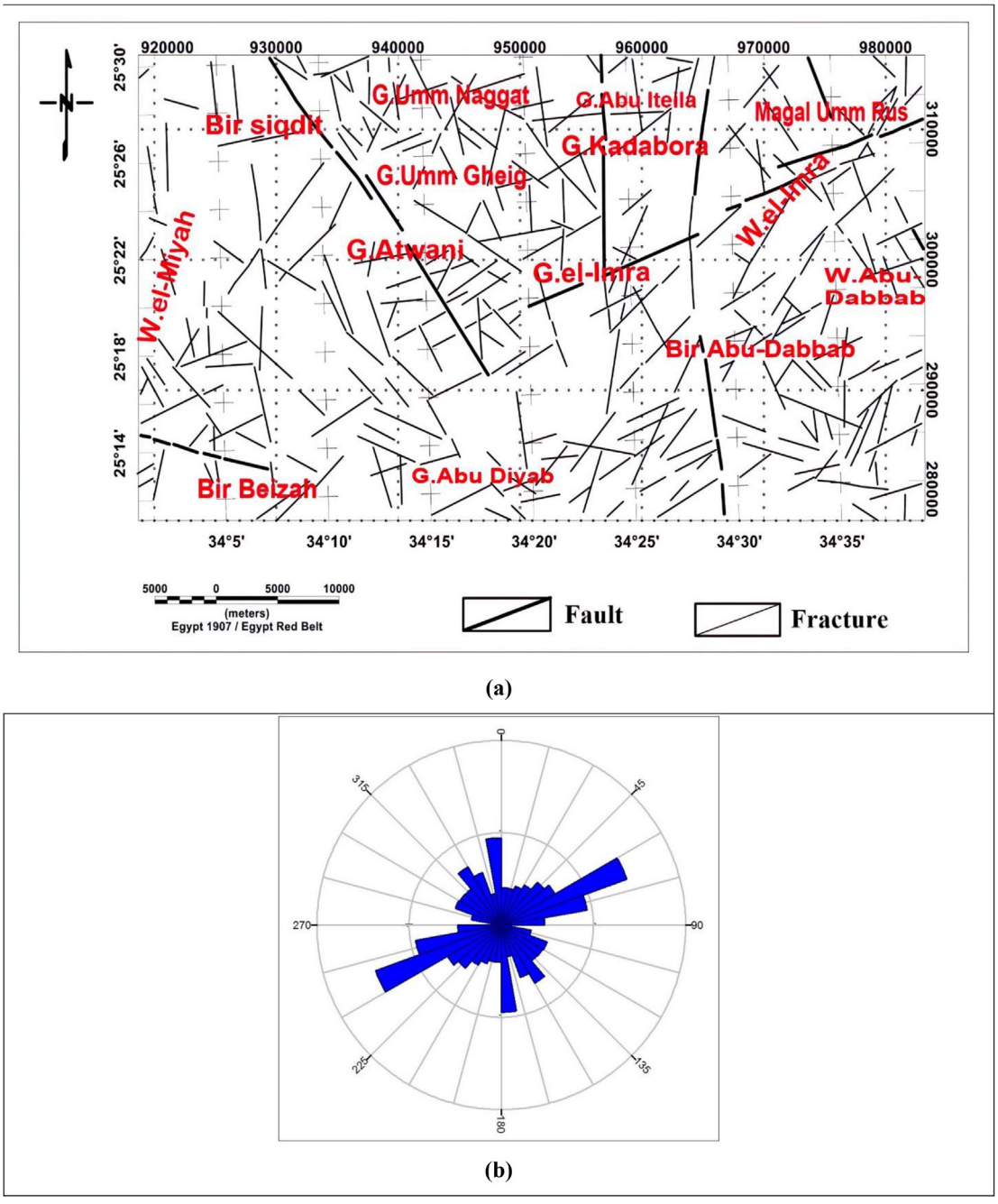

Fig. 3. (a) Geologic fault trends and fractures derived from the geologic map of the study area in Fig. (1) and (b) Rose diagram of geologic lineaments of the study area (Conoco, 1987).

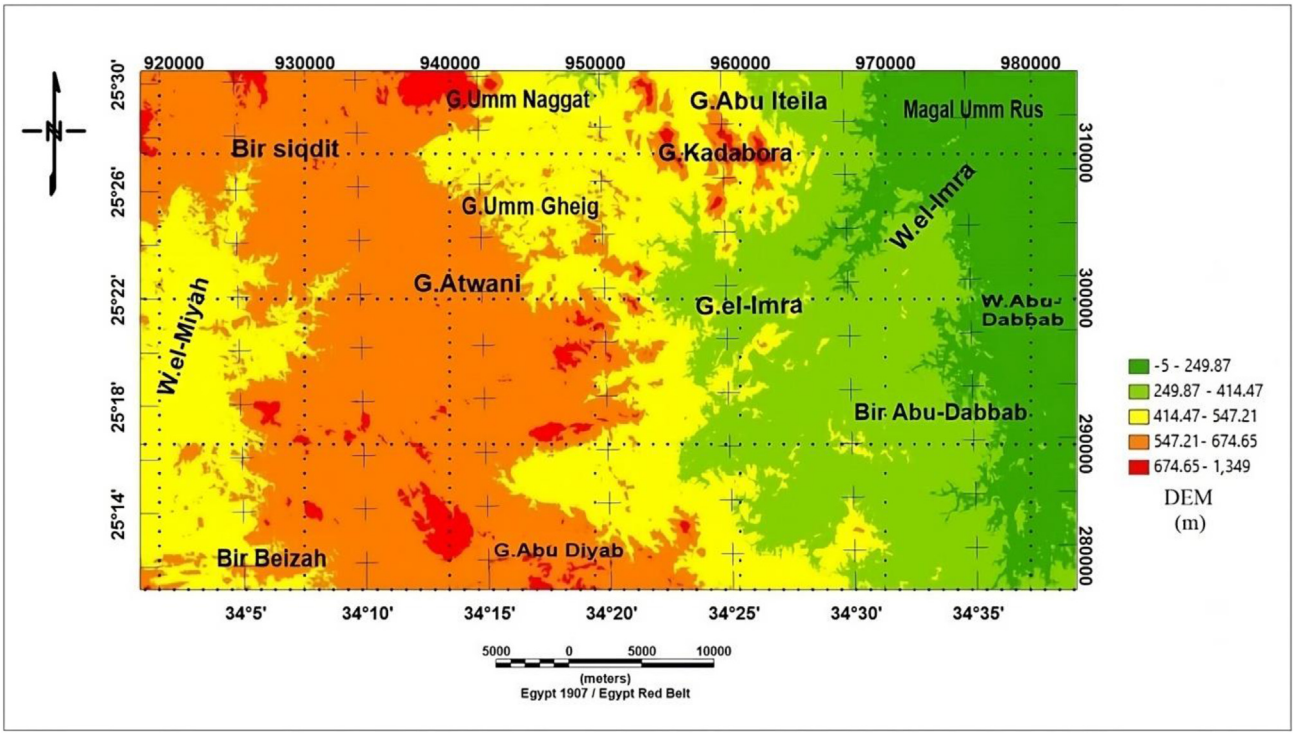

Fig. 4. Digital Elevation Model (DEM) of the study area (http://earthexplorer.usgs.gov).

3. Methodology

3.1. Remote sensing and digital elevation model

This study has used remote sensing technique with geographic information system (GIS) as important tools for surface analysis for many objectives like topographic information and tracing surface linear features using the Shuttle Radar Topography Mission (SRTM), launched by NGA and NASA. SRTM research effort has led to the formulation of the Digital Elevation Models (DEM) from which a high-resolution digital topographic database of Earth can be obtained (Nikolakopoulos

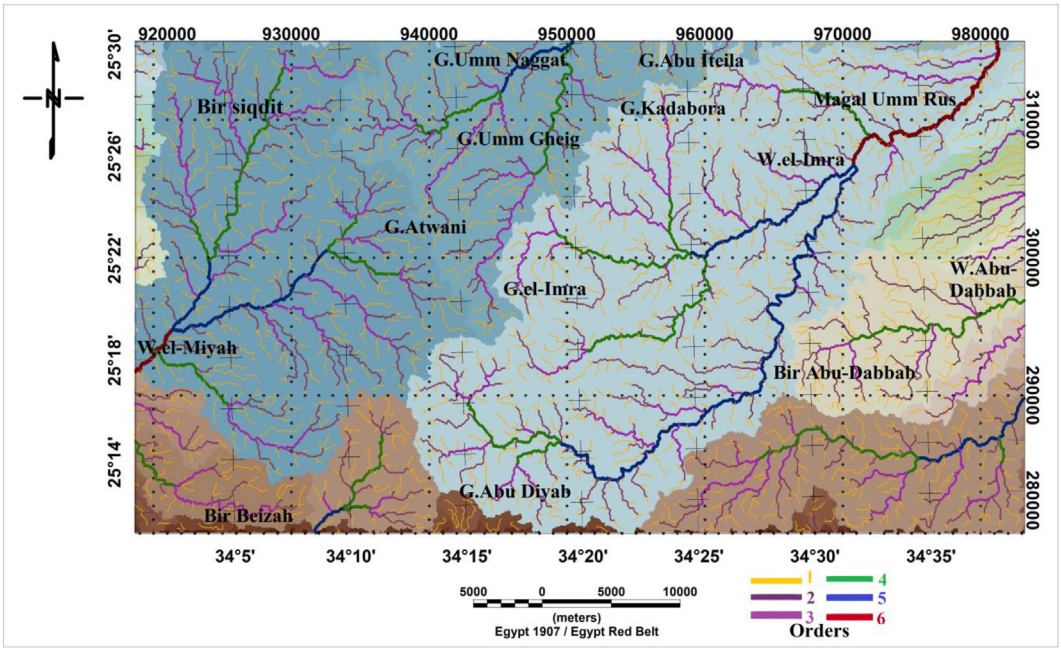

Fig. 5. Stream order within the basins of the study area.

et al., 2006). The Digital Elevation Model representing the surface of the area under investigation has been downloaded from http://earthexplorer.usgs.gov.

3.2. Airborne gamma-ray spectrometry

The study is based on the analysis of sheets no. 71 and 72 of the spectrometric measurements carried out from 1982 to 1984 through the Mineral, Petroleum, and Groundwater Assessment Project (MPGAP); the airborne gamma-ray spectrometric survey was flown along a set of parallel traverse flight lines oriented in a northeast–southwest direction with an azimuth of 45° and 225° from the true north. The flight line spacing was 1 km. The tie lines were oriented in a northwest–southeast direction with an azimuth of 135° and 315° with a

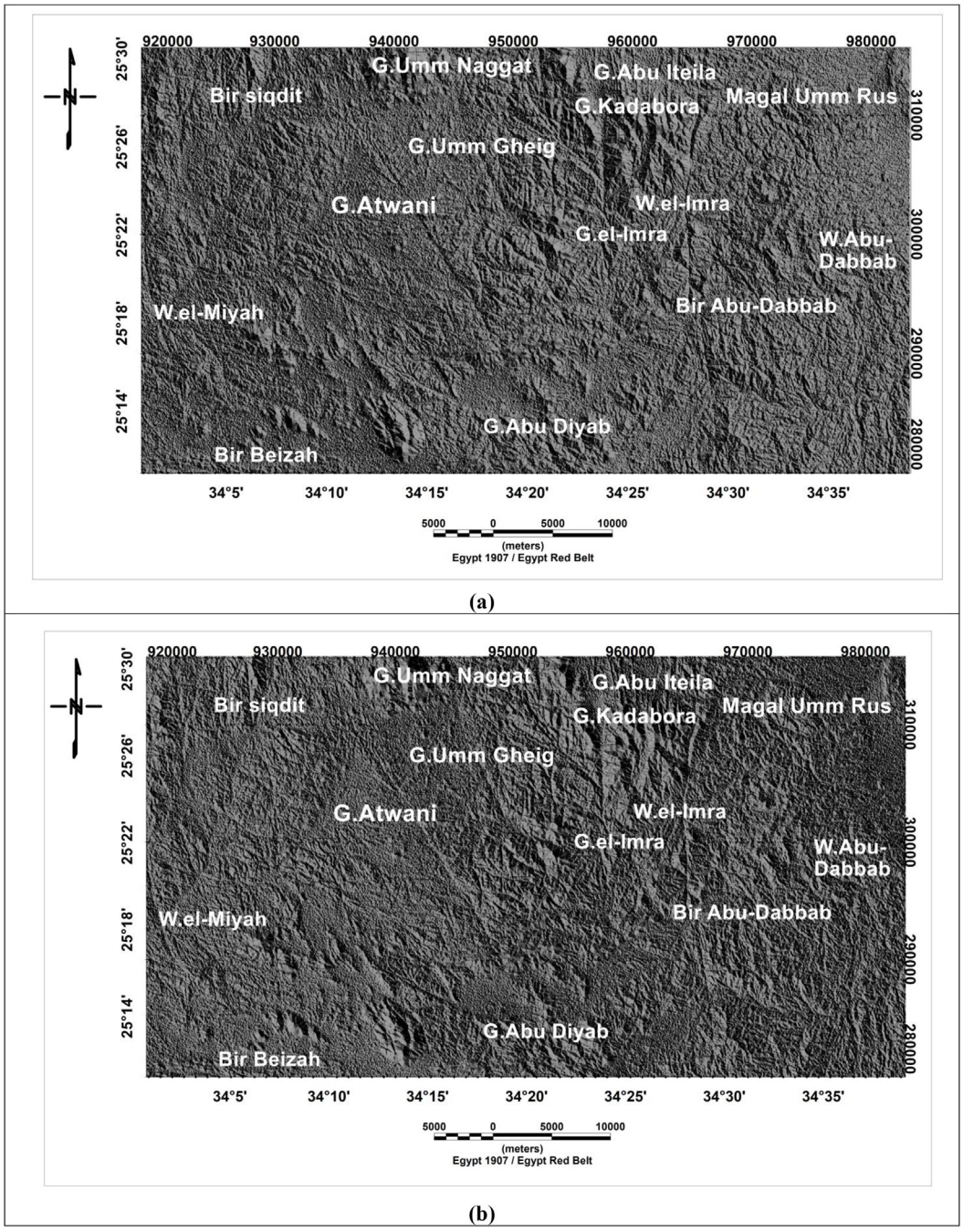

Fig. 6. (a) Shaded relief image created by combining four shaded relief images with sun angles of 0°, 45°, 90°, and 135°. (b) Shaded relief image created by combining four shaded relief images with sun angles of 180°, 225°, 270°, and 315° of the study area.

spacing of 10 km. Survey flying was done at a mean terrain clearance of 120 m with an aircraft average speed ranging from 220 to 315 km/h. The collected spectral gamma-ray measurements were corrected, compiled, and finally displayed as contour maps (Aero-Service, 1984).

Gamma-ray spectrometric signatures of rocks can be used to delineate their lithologies and structures (Darnley, 1973). Airborne gamma-ray spectrometric survey of the study area provided information on four parameters (variables): these are the total count of gamma radiation (T.C in μR/h), absolute concentrations of the three radioelements: potassium (K in %), equivalent uranium (eU in ppm), and equivalent thorium (eTh in ppm). In addition to these variables, three radioelement ratios, eU/eTh,

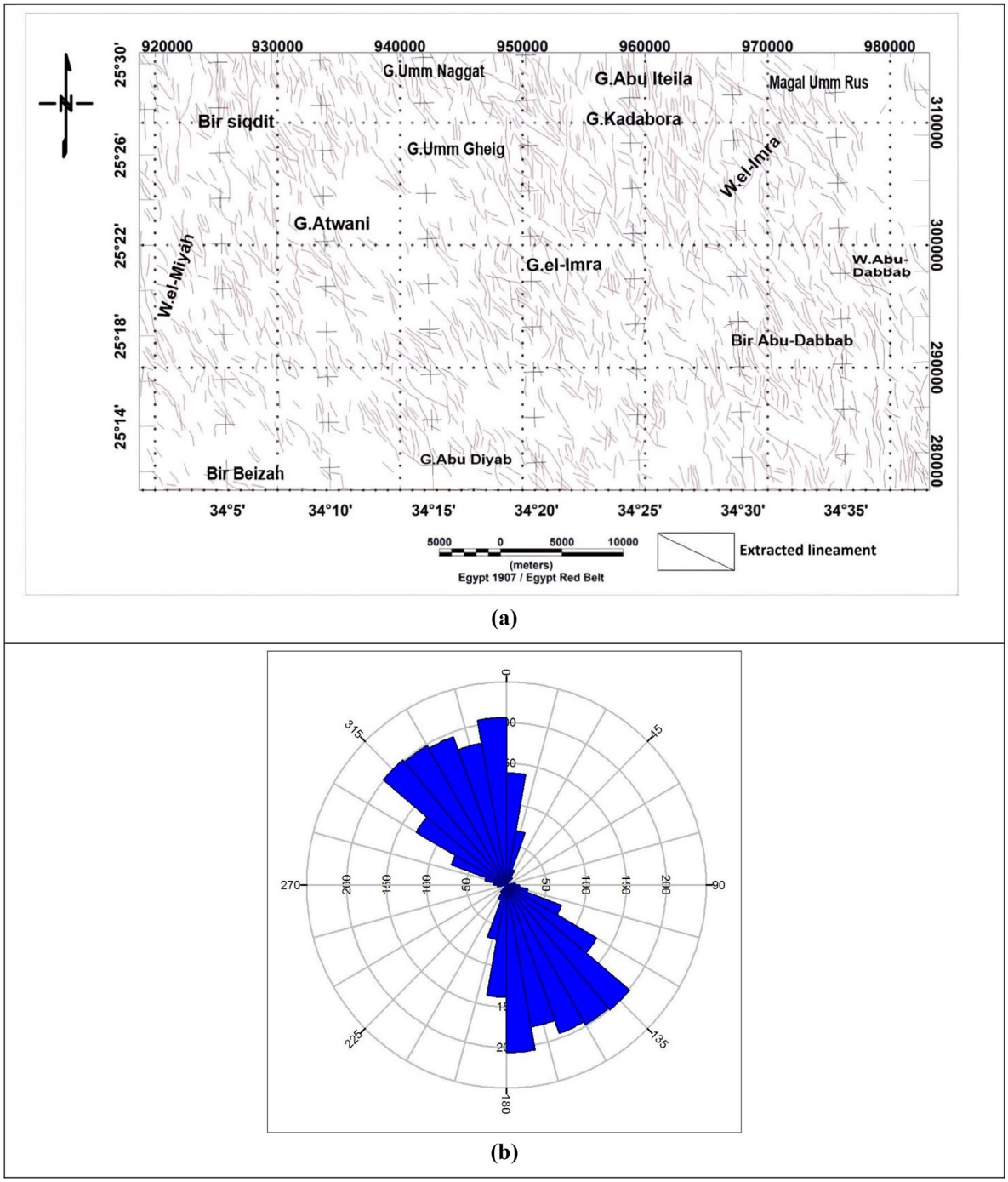

Fig. 7. (a) Automatic lineament map of combining four shaded relief images with sun angles of 0°, 45°, 90°, and 135° and (b) Rose diagram of the automatic lineament map of the study area.

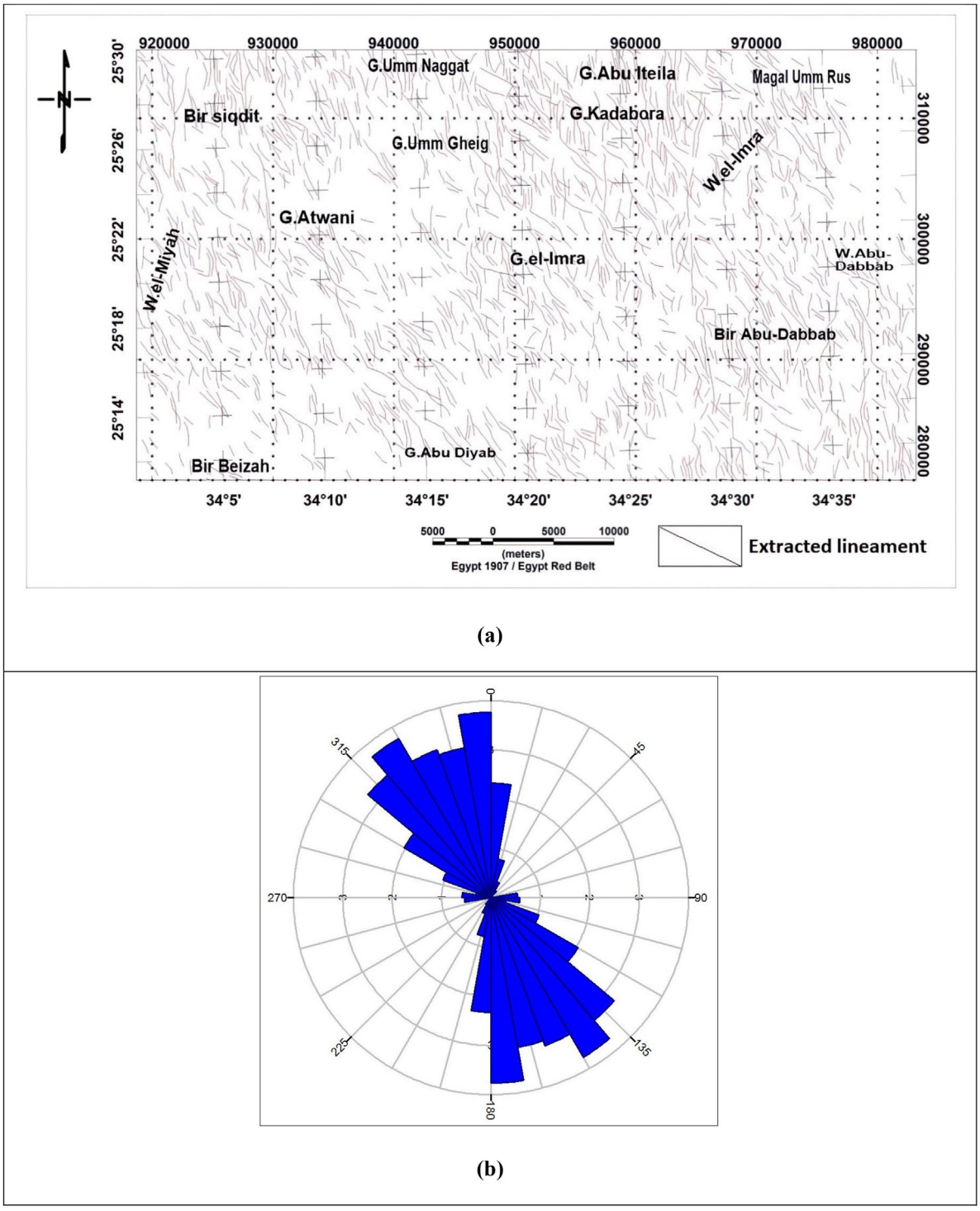

Fig. 8. (a) Automatic lineament map of combining four shaded relief images with sun angles of 180°, 225°, 270°, and 315° and (b) Rose diagram of the automatic lineament map of the study area.

eU/K, and eTh/K, were computed to visualize the relative concentrations of the radioelements.

4. Results and discussion

4.1. Surface analysis using remote sensing and GIS techniques

4.1.1. Elevation analysis

Analysis of DEM shows a gradual variation in elevations from west to east, where the highest elevations (more than 500 m) dominate in the western and central parts of the map, except Wadi El-Miyah (Fig. 4). In comparison, the lowest elevation (less than 500 m) exists in the eastern part of the area, which overlooks the Red Sea coast.

Stream ordering is the basic parameter of the quantitative analysis of the drainage (Pareta and Pareta, 2012). The resulting stream network extracted from an elevation model in the study area contains six main orders forming five basins, each one is discriminated by a different color as shown in Fig. 5.

4.1.2. Lineament extraction

Eight shaded relief images with light sources originating from eight particular directions were created to determine the linear topographic features from the DEM. The first shaded relief image has a solar azimuth (sun angle) of 0°, the other seven shaded relief images were obtained with seven illumination directions: 45°, 90°, 135°, 180°, 225°, 270°, and 315°.

The GIS overlay technique is used to compute the combinations of the four shaded relief maps into one image. The first four shaded relief images are overlaid to create a single image with multi-illumination directions (0°, 45°, 90°, and 135°) and the other with illumination directions (180°, 225°, 270°, and 315°) (Fig. 6a and b). Then, the combined images were employed for automatic lineament extraction throughout the study area (Figs. 7 and 8). Inspection of the obtained lineament pattern shows that the main trends take mostly the NW–SE and N–S directions, which coincide with Gulf of Suez trend.

4.2. Interpretation of gamma-ray spectrometry

4.2.1. Qualitative interpretation of the spectrometric maps

The qualitative interpretation of the spectrometric survey data depends mainly upon the correlation between the general pattern and surface distribution of the spectrometric measurements and the various rock-type units recorded in the geological map, for example, faults and certain lithological contacts may be manifested by disruption of the contours of the spectrometric maps. Furthermore, faults sometimes exhibit radioactive highs due to increased permeability, allowing access to the migrating radon. Other faults show a radioactive low because of the increased leaching of radioactive

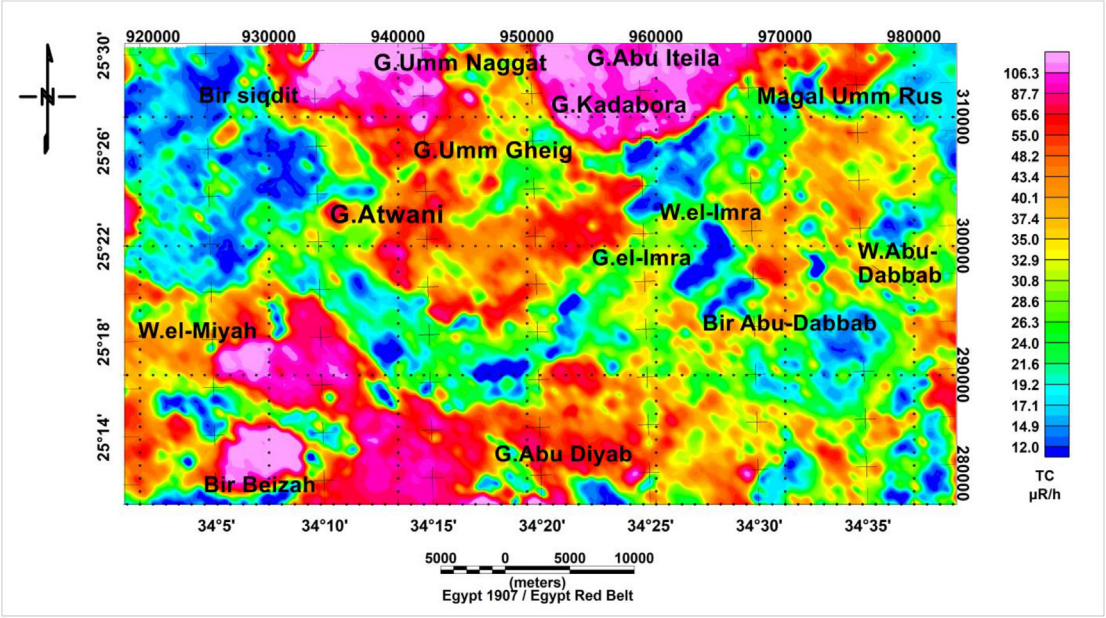

Fig. 9. Fill-colored contour map of total count (T.C) in μR/h of the study area.

minerals along fault zones (Abd El-Nabi, 1990). The following paragraph shows the behavior of radiometric parameters in the study area.

4.3. Total count (TC) contour map

Investigation of the total count (TC) map of the study area (Fig. 9) illustrates three different concentration levels. The first level (low concentration) is less than 24 μR/h that dominates at the NW, SW, SE, and NE directions, with some scattered points in the central parts of the area that are characterized by the presence of Ophiolitic Serpentinite, Metavolcanics rocks, and some Quaternary and Wadi deposits. The second level ranges from 24 to 50 in μR/h and is mostly observed in Metagabbro to Metadiorite rocks, Metasediments, Hammamat clastics, Gabbroic rocks, and some parts of

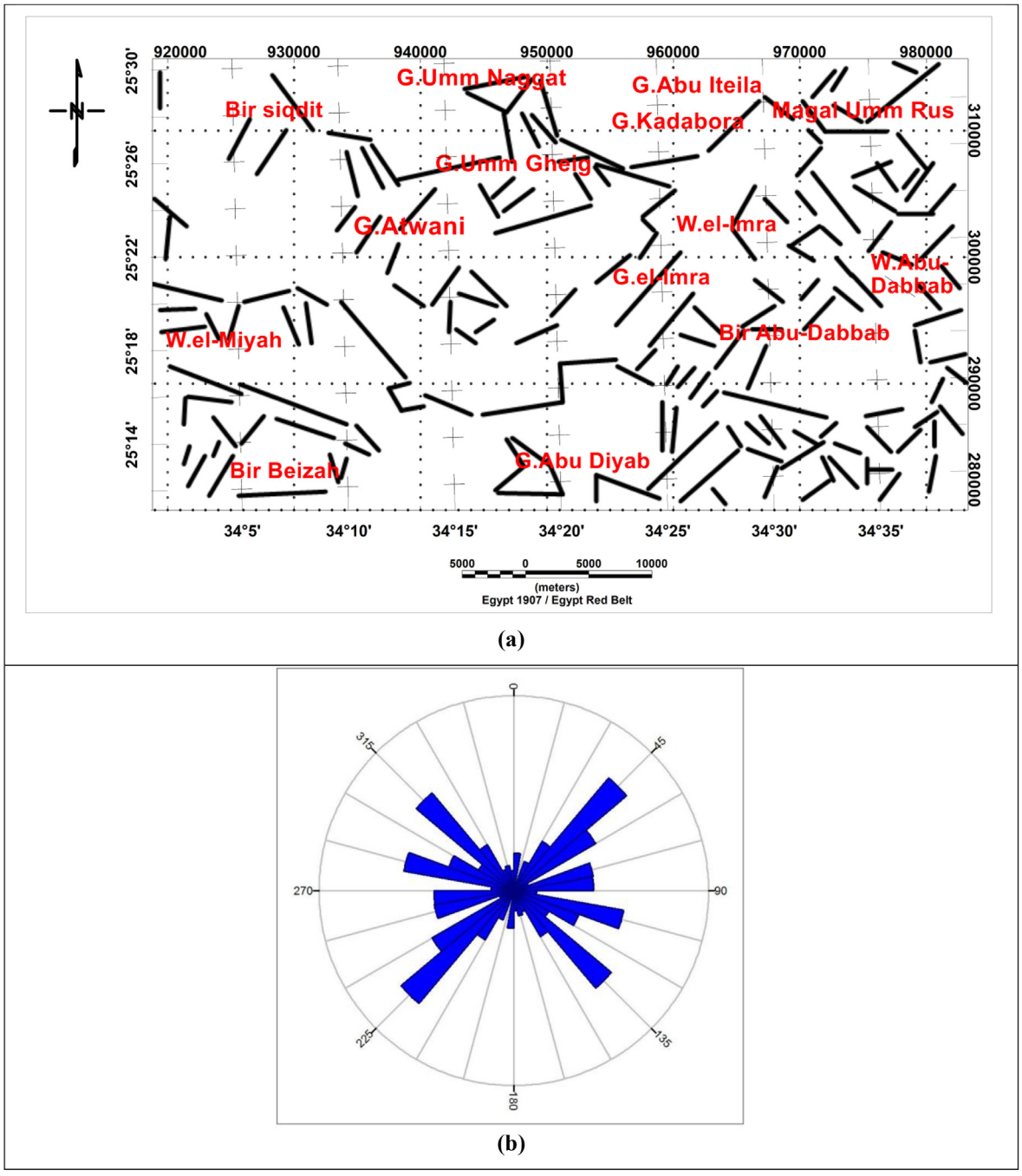

Fig. 10. (a) Extracted lineaments from total count (T.C) map and (b) Rose diagram of the extracted lineaments of the study area.

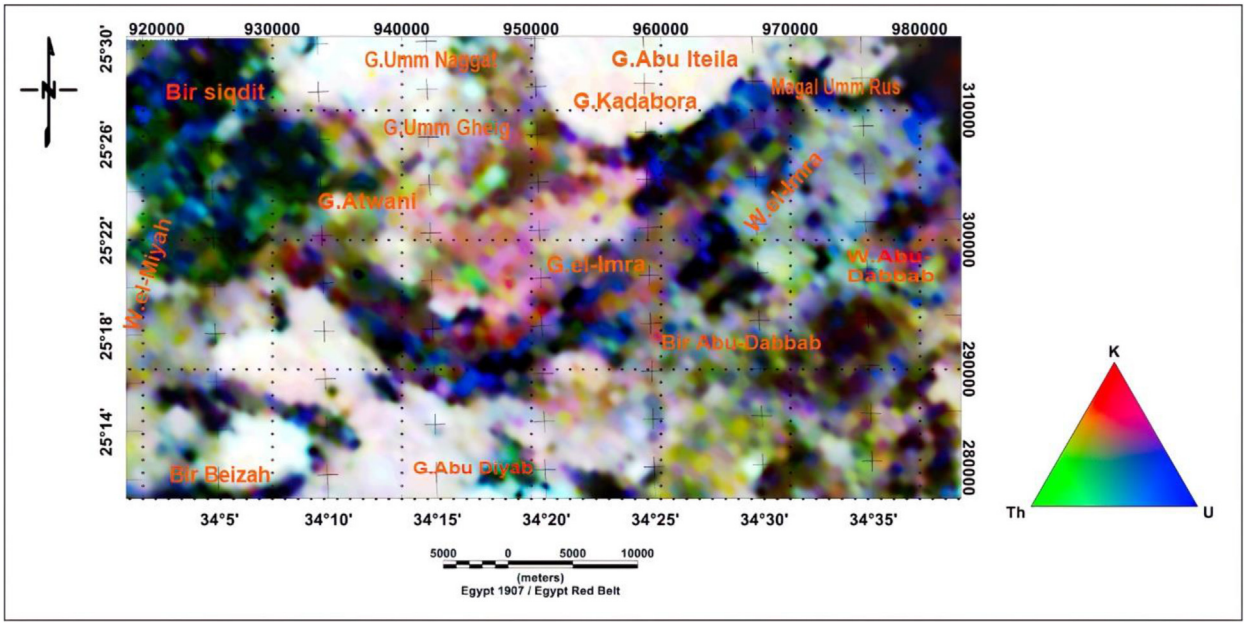

Fig. 11. False color absolute radioelements (K, eU, and eTh) composite image map of the study area.

Quaternary and Wadi deposits at the eastern part and some dispersed points in the central part of the region. The third level exceeds 50 in μR/h, which reflects the presence of granitic rocks at the northern, southwestern, southern, and central parts of the study area. Fig. 10 shows lineament directions derived from spectrometric data indicating NW–SE and NE–SW trends. This lineament pattern includes the rock boundary effect, therefore, it differs from that obtained from RS data.

4.4. Composite image maps

4.4.1. Radioelement composite image map

The radioelement composite image map (Fig. 11) shows the concentration in the three radioelements, which mainly reflects lithologic variations. This map is a three-element display of the equivalent uranium (ppm), equivalent thorium (ppm), and potassium (%). The color index at each corner of the triangular legend (K in red, eU in blue, and eTh in green)

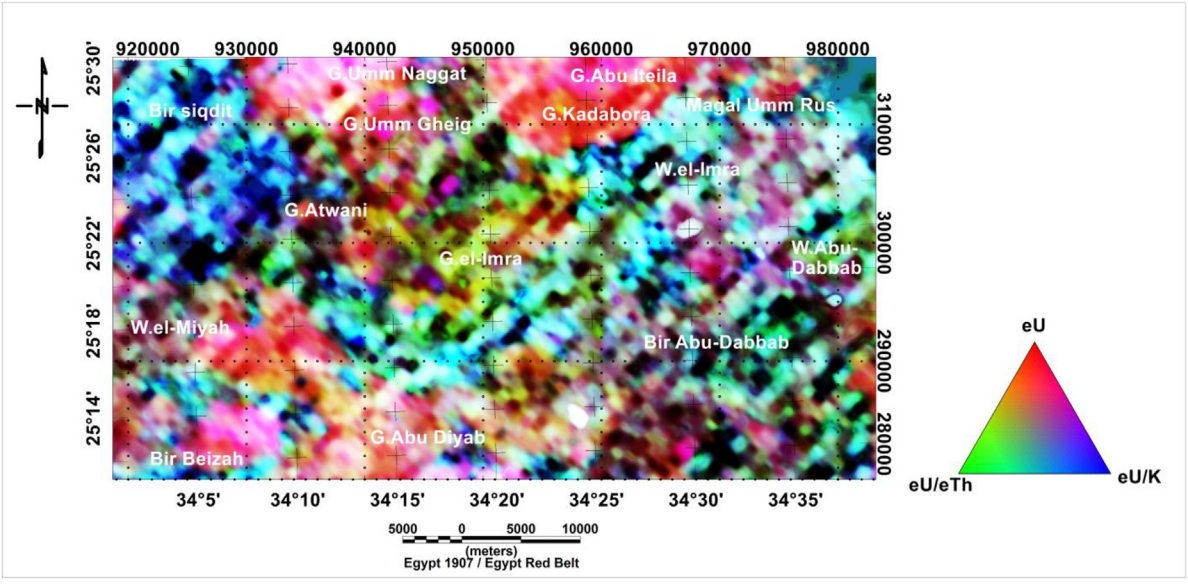

Fig. 12. False color equivalents' uranium (eU, eU/K, and eU/eTh) composite image map of the study area.

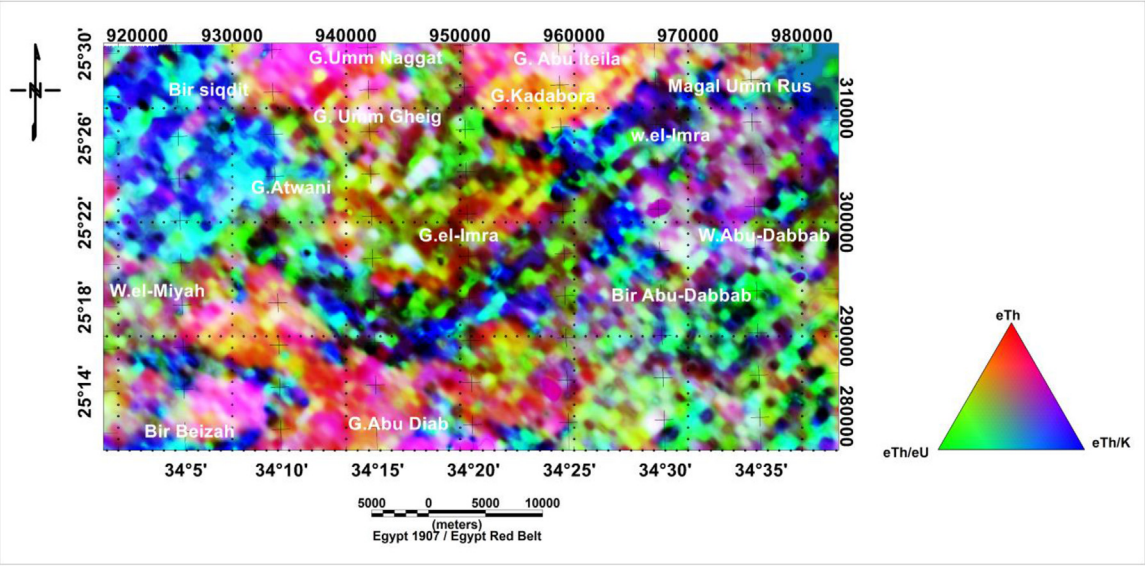

Fig. 13. False color equivalents' thorium (eTh, eTh/K, and eTh/eU) composite image map of the study area.

indicates a 100% concentration of the indicated radioelements. The eU, eTh, and K images emphasize the radioelements and the high light parts, where the particular radioelement has relatively higher concentrations.

It is noticed that the higher light zones are correlated with Granitic rocks in the northern, SSW, and southern parts of the map. The low eU, eTh, and K concentrations (the black part) show scattered spots correlated with the Ophiolitic Serpentinite at the eastern and SW parts, Metagabbro to Metadiorite rocks at northern, SE, and SW parts, and Metavolcanics rocks and Metasediments at the northwestern, central, and eastern parts, in addition to Quaternary deposits, which lie at the northeastern side of the study area.

4.4.2. Equivalent uranium composite image map

The equivalent uranium composite image map (Fig. 12) reflects three components: eU (in red) with the ratios of eU/eTh (in green) and eU/K (in blue). The relative concentration of uranium concerning potassium and thorium is an important diagnostic factor in recognizing possible uranium deposits (IAEA International Atomic Energy Agency, 1988). The bright areas reflect anomalous zones of uranium

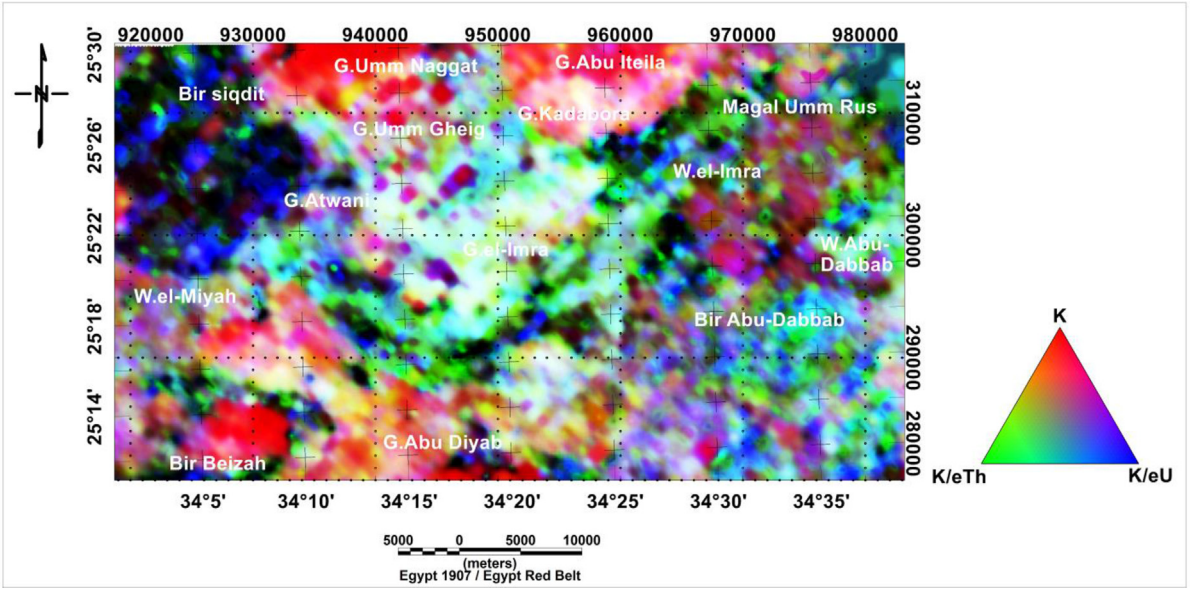

Fig. 14. False color potassium (K, K/eTh, and K/eU) composite image map of the study area.

Table 1. Statistics of airborne spectrometric data overall the study area.

Variables	Minimum	Maximum	X	Σ	CV (%)
T.C (μR/h)	1.86	184.58	41.6	28.05	67.5
eU (ppm)	0.11	11.25	1.7	1.3	78.3
eTh (ppm)	0.4	29.33	4.06	3.03	74.6
K (%)	0.08	4.07	1.23	0.8	64.64
eU/eTh	0.06	3.03	0.42	0.15	35.16
eU/K	0.22	14.6	1.42	0.61	42.97
eTh/K	0.96	11.98	3.4	0.91	26.77

Explanation: %, percent; **CV (%)**, coefficient of variability; eTh, equivalent thorium in ppm; **eU**, equivalent uranium in ppm; **K**, potassium in %; **ppm**, part of radioactive material per million pairs of rock; **T.C**, total count in μR/h; **X**, arithmetic mean; **μR/h**, microroentgen per hour and **σ**, standard deviation.

concentration, which correlate with Granitic rocks and Wadi deposits in northern, southern, and southwestern parts of the investigated area. Meanwhile, low uranium values (dark areas) show scattered spots that correlate with the Ophiolitic Serpentinite, Metavolcanics rocks, some parts of intrusive Metagabbro to Metadiorite rocks, and Shagara Formation in western, southeastern, and northeastern parts of the study area.

Table 2. Varimax factor loading matrix for the seven spectrometric variables of the study area.

Variables	Component		
	F1	F2	F3
T.C (μR/h)	0.997	−0.037	−0.013
eU (ppm)	0.942	0.237	0.144
eTh (ppm)	0.971	−0.071	0.195
K (%)	0.957	−0.119	−0.198
eU/K	0.20	0.858	0.498
eTh/K	0.046	0.040	0.995
eU/eTh	−0.027	0.981	−0.166

4.4.3. Equivalent thorium composite image map

The equivalent thorium composite image map (Fig. 13) includes eTh (in red), eTh/eU (in green), and eTh/K (in blue). The bright-colored zones reflect the areas of thorium enrichment associated with Granitic rocks, Quaternary, and Wadi deposits at northern, southern, and central parts of the area. The low thorium values (represented by dark areas) are associated with the Ophiolitic Serpentinite, Metavolcanics rocks, Metasediments, Um Mahara, and Ranga formations located at the

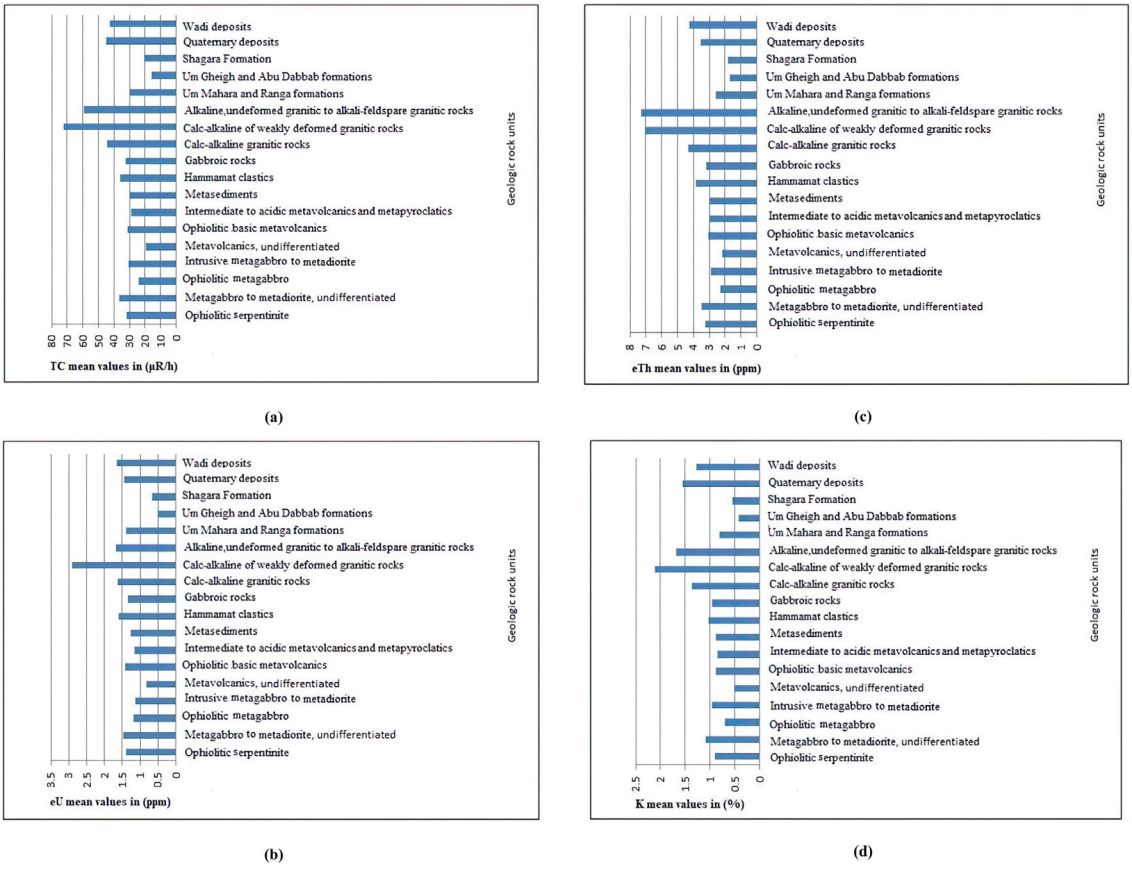

Fig. 15. Frequency distribution histograms of mean value of radio elements in geologic rock units in the study area: a) T.C, b) eU, c) eTh, and d) K.

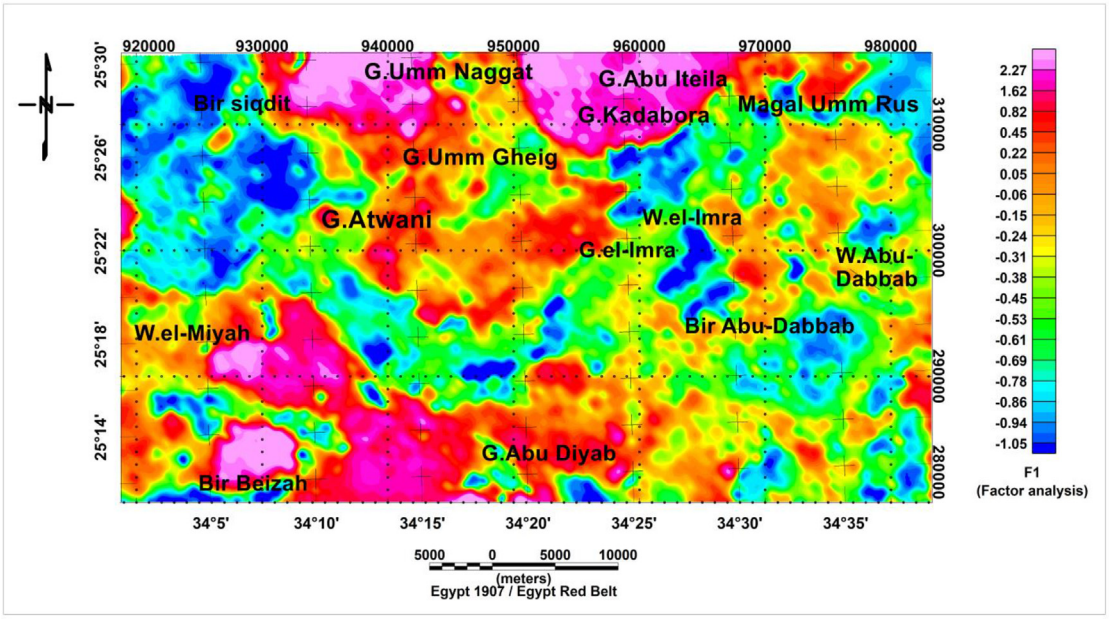

Fig. 16. Filled color contour map of the first factor (F1) map of the study area.

western, northeastern, and central parts of the study area.

4.4.4. Potassium composite image map

The potassium composite image map (Fig. 14) combines K% (in red) with K/eTh (in green) and K/eU (in blue), which showed the relative distribution of potassium concentration. The low K% values (represented by dark areas) are associated with the Ophiolitic Serpentinite, ophiolite Metagabbro, and Metavolcanics rocks at the northwestern, northeastern, and scattered parts in central area of the map. The bright areas reflect the potassium concentration that seems to belong to Granitic rocks and some parts of Quaternary deposits at the northern, southern, and central parts of the map.

4.4.5. Quantitative interpretation of the spectrometric maps

The quantitative interpretation depends principally upon the fact that the absolute and relative concentrations of the radioelements (K%, eU, and

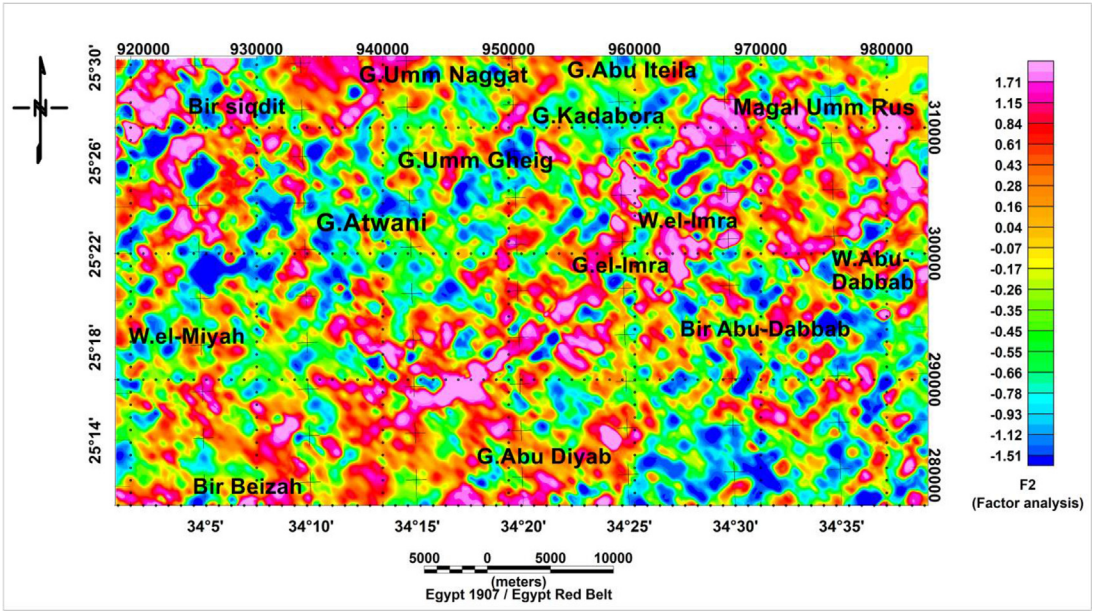

Fig. 17. Filled color contour map of the second factor (F2) map of the study area.

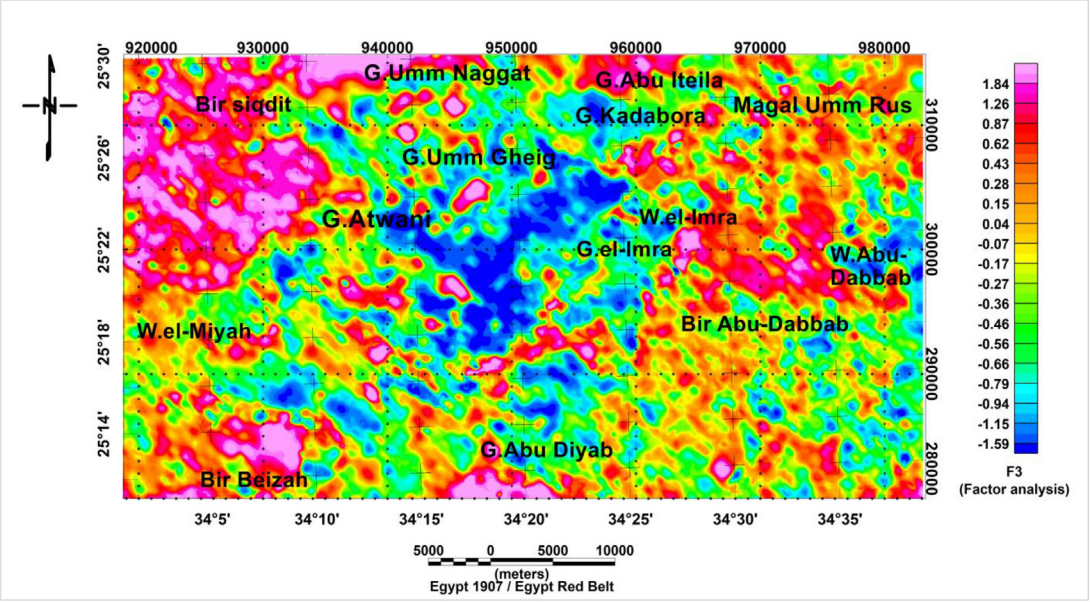

Fig. 18. Filled color contour map of the third factor (F3) map of the study area.

eTh) vary measurably and significantly with lithology (Darnely and Ford, 1989). The quantitative treatment of the spectrometric data in this study is discussed in light of statistical treatment. The collected spectrometric data (T.C, eU, eTh, and K%) are in the form of digital grids, from which three ratios (eU/eTh, eU/K%, and eTh/K%) were calculated. Standard statistics were applied to the raw data to compute means, minima, maxima, standard deviations, and normality check for each variable (Table 1). The statistical analysis was applied on the seven variables (T.C, eU, eTh, K%, eU/eTh, eU/K%, and eTh/K%) of each rock unit, according to the detailed geological map of the study area. The statistical treatment of the airborne gamma-ray spectrometric data depends mainly on the application of

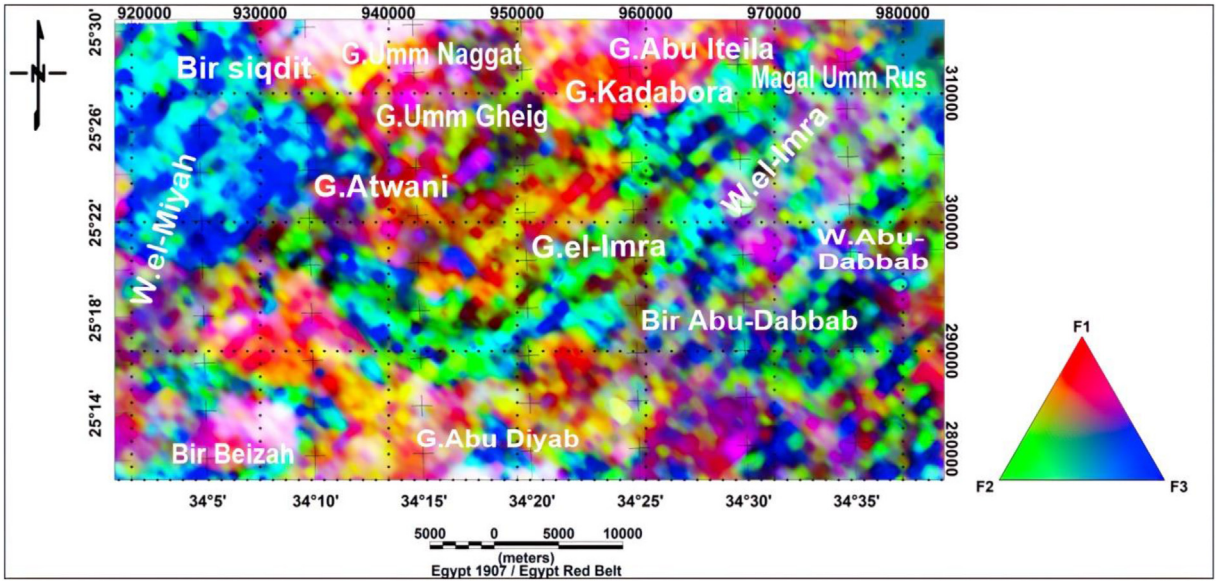

Fig. 19. Composite map of F1, F2, and F3 factor scores of the study area.

the coefficient of variability (CV %) technique. For a certain variable value in the study area, if the (CV%) is less than 100 %, the variables tend to exhibit normal distribution, according to equation (1)

$$CV\ \% = (\sigma / X) \times 100 \quad (1)$$

where σ is the standard deviation and X is the arithmetic mean.

4.4.6. Relationship between radioactivity and lithology

Fig. 15 shows seven statistical parameters represented by the frequency histogram distributions of mean values of a) T.C (μR/h), b) eU (ppm), c) eTh (ppm), and d) K (%) in all geologic rock units in the study area, it is noted that high mean values occur mainly in granitic rocks.

4.4.7. Remapping of geologic map based on statistical analysis and radioactivity maps

i) Factor analysis technique (statistical analysis)

All variables (T.C, eU, eTh, K, eU/K, eTh/K, and eU/eTh) are subjected to statistical analysis and reduced without significant loss of information into three factors, as shown in Table 2.

In the following section, we are going to give a detailed discussion of factor one (F1) (Fig. 16), factor two (F2) (Fig. 17), and factor three (F3) (Fig. 18) for the study area. Rocks that have high values of F1 are represented by older and younger Granitic rocks, some parts of Quaternary deposits, and Wadi deposits at the northern, SSW, southern, and central parts of the study area. Meanwhile, the high levels of F2 are related to older and younger Granitic rocks at the northern, SSW, southern, and central part of

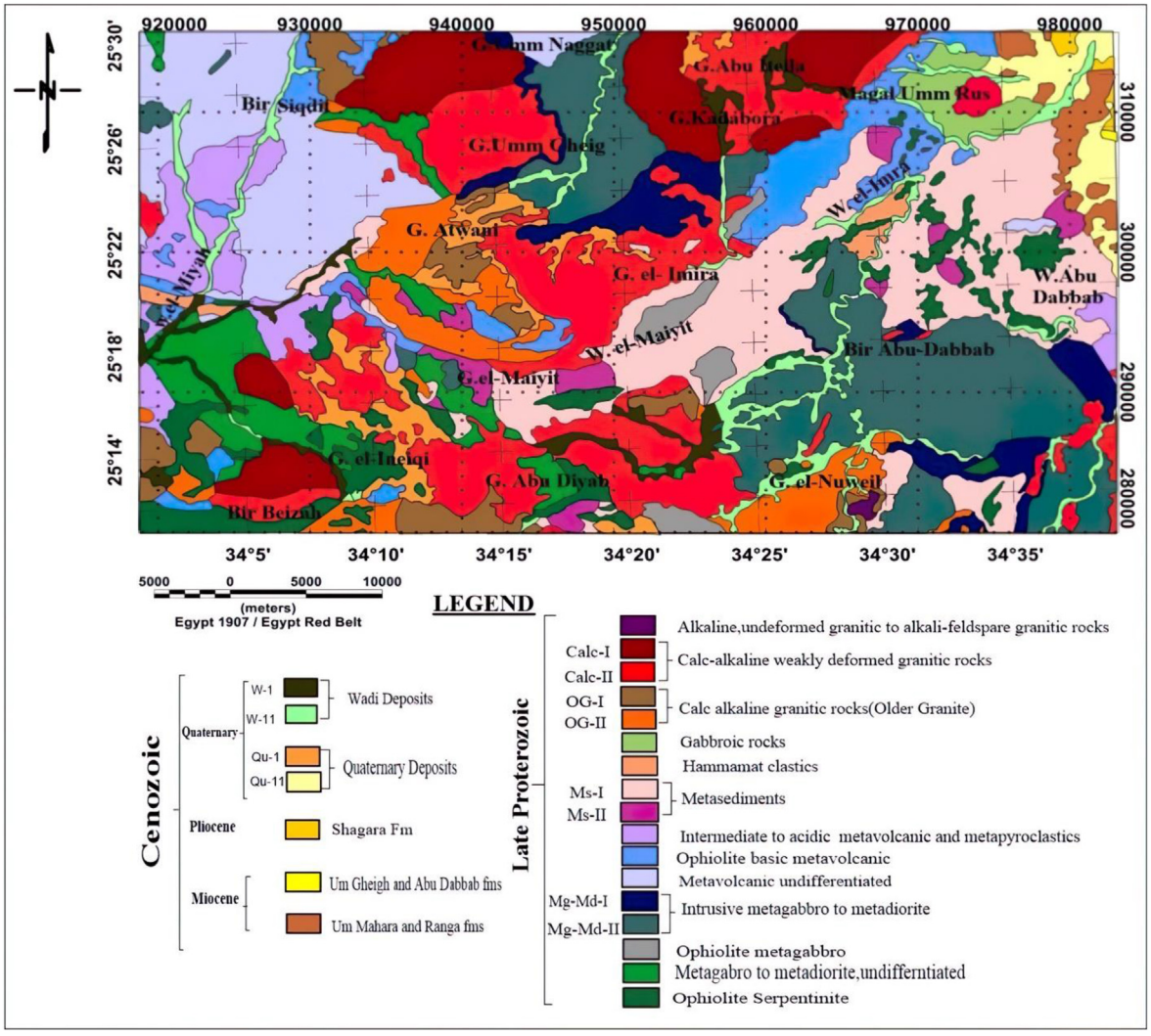

Fig. 20. Interpreted radiometric rock units' map of the study area.

the study area, some parts of Ophiolitic Serpentinite at southwestern and eastern parts of the area, Metavolcanics rocks at the northwestern part of the map, and Metasediments at northeastern to central parts of the study area. This is in addition to the rock units overlooking the Red Sea coast, including Um Mahara and Ranga formations, Quaternary, and Wadi deposits, the high levels of factor F3 are found in older and younger Granitic rocks at the northern, SSW, southern, and central parts of the study area, Metavolcanics rocks at northwestern part of the map, and some parts of Metasediments at northeastern to central parts of the area. This is in addition to the rock units overlooking the Red Sea coast, including Um Mahara and Ranga formations, Quaternary, and Wadi deposits. Fig. 19 shows the composite factorization map. Inspection of this map indicates that the results obtained through the application of the factor analysis technique made it possible to delineate the geologic units of the study area, which shows a relative similarity to the geologic map (Fig. 2).

ii) Radioactivity maps

According to comparison of higher radioactivity levels in the Total Count map (Fig. 9) and scores of the factor analysis technique with the geologic map (Fig. 2), six rock units dominate, each of them is divided into two types (Fig. 20) as follows: 1) Intrusive Metagabbro to Metadiorite (Mg–Md-I and Mg–Md-II), 2) Metasediments (Ms-I and Ms-II), 3) Calc-alkaline granitic rocks (OG-I and OG-II), 4) Calc-alkaline of weakly deformed granitic rocks (Cal-I and Cal-II), 5) Quaternary deposits (Qu-I and Qu-II), and 6) Wadi deposits (W–I and W-II). The other rock units remain as they were.

4.4.8. Identification and outlining the uraniferous provinces

The aim of aerial prospection utilizing gamma-ray spectrometric survey is mainly for delineating expected boundaries of potential uraniferous locations with variable rock units that have high concentrations of uranium (Saunders and Potts, 1976). The most important parameters that can be measured are relative concentrations of uranium to thorium and uranium to potassium, in conjunction with uranium measurements. These parameters can lead to identifying anomalous areas of uranium concentration (Darnley, 1973).

In this study, appropriate zones for uranium prospecting are chosen based on the calculation of probabilities, where the data vary from the mean background as provided by the data themselves. These variations were computed in terms of specific levels of probabilities. The threshold value, which marks the start of the high anomalous values, was defined as the value of two standard

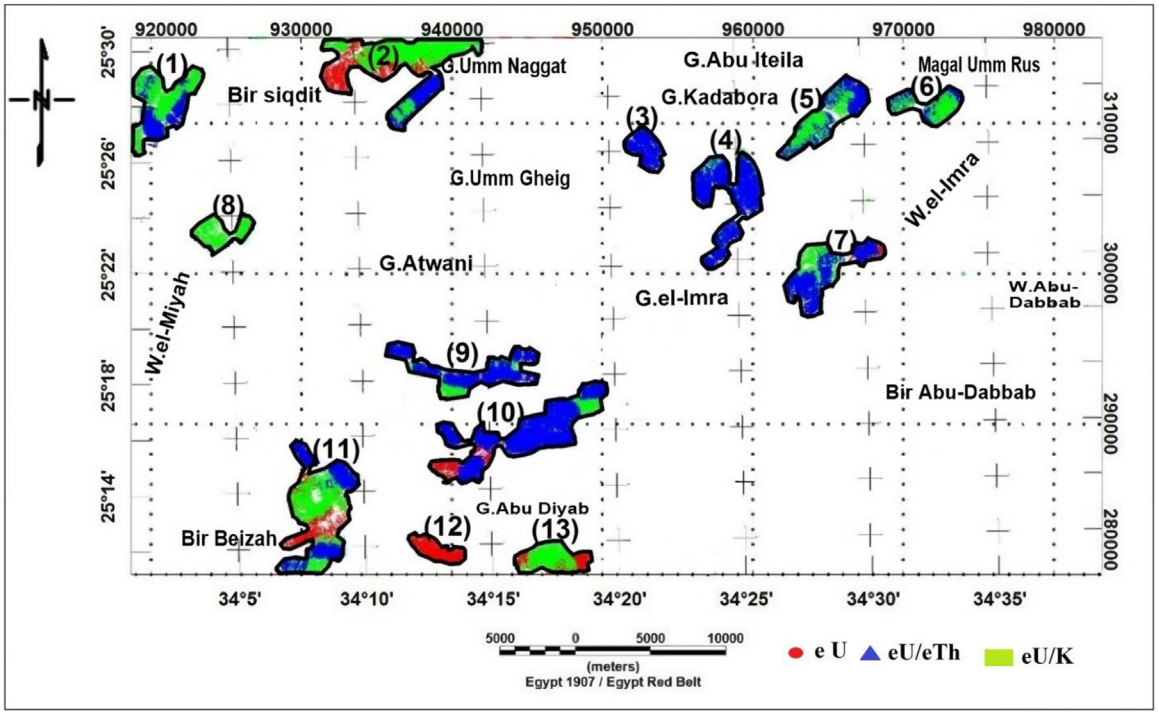

Fig. 21. Locations of uraniferous concentrations of the study area.

Table 3. Anomalous location of eU, eU/eTh, and eU/K in the study area.

Anomaly group no	Coordinate of anomaly center				Trend	Rock type
	X	Y	Lat	Long		
1	920400	311100	25° 27' 59.6"	34° 2' 9.22"	NE–SW	Metavolcanics rocks
2	935600	314600	25° 29' 41.63"	34° 11' 15.52"	E–W	Granitic rocks
	937300	311600	25° 28' 2.97"	34° 12' 13.71"	NE–SW	Granitic rocks
3	952700	308400	25° 26' 6.85"	34° 21' 21.2"	N–S	Granitic rocks and some parts of Intrusive metagabbro to metadiorite
4	956900	306200	25° 24' 52.03"	34° 23' 49.24"	NE–SW	Wadi deposits and some parts of Intrusive metagabbro to metadiorite
	958700	304000	25° 23' 39.17"	34° 24' 51.52"	NE–SW	Ophiolitic Metagabbro and Ophiolitic basic metavolcanics
5	964800	310500	25° 27' 4.9"	34° 28' 35.4"	NE–SW	Ophiolitic basic metavolcanics and Granitic rocks
6	971500	311000	25° 27' 15.39"	34° 32' 35.24"	E–W	Gabbroic rocks
7	963900	300300	25° 21' 34.81"	34° 27' 53.79"	NE–SW	Serpentinite, Intrusive metagabbro to metadiorite, and Hammamat clastics
8	924500	302600	25° 23' 20.72"	34° 4' 28.77"	E–W	Metavolcanics rocks and Wadi deposits
9	940900	233100	25° 17' 59.92"	34° 14' 6.36"	E–W	Granitic rocks
10	943800	289100	25° 15' 47.86"	34° 15' 46.38"	NE–SW	Metagabbro to metadiorite and Metasediments
11	931200	283100	25° 13' 15.37"	34° 8' 12.62"	N–S	Metagabbro to metadiorite, Granitic rocks, and Wadi deposits
12	939000	281500	25° 11' 45.03"	34° 12' 48.63"	NW–SE	Granitic rocks
13	946500	281300	25° 11' 32.65"	34° 17' 15.9"	E–W	Metasediments

deviations above the calculated arithmetic mean value (X+2σ) for all individual points in every rock unit for eU, eU/eTh, and eU/K measurements. Thirteen groups of statistically significant (anomalous) zones can be detected, and the anomalous locations of eU, eU/eTh, and eU/K are summarized in Fig. 21 and Table 3.

4.5. Conclusions

Several methods represented by field geology, DEM, and spectrometric method shave been used to detect surface lineaments in the study area. The study shows three main trends: NW–SE, NE–SE, and N–S. The higher mean values of T.C (μR/h), eU (ppm), eTh (ppm), and K (%) occur mainly in Granitic rocks of the study area. When remapping of the geologic map based on scores of the factor analysis technique and radioactivity maps, six rock units dominate, each of them is divided into two types: 1) Intrusive Metagabbro to Metadiorite (Mg–Md-I and Mg–Md-II), 2) Metasediments (Ms-I and Ms-II), 3) Calc-alkaline granitic rocks (OG-I and OG-II), 4) Calc-alkaline of weakly deformed granitic rocks (Cal-I and Cal-II), 5) Quaternary deposits (Qu-I and Qu-II), and 6) Wadi deposits (W–I and W-II). Identification of valuable radiometric anomalies carried out by calculating the significant factor (X+2σ) for eU, eU/eTh, and eU/K measurements for all individual points in every rock unit indicates the presence of 13 groups characterized by high uraniferous concentrations, and distributed in the NW, NE, and southern parts of the study area. Correlation between uraniferous zones and lineament distribution shows that some high uraniferous parts exist where high lineament density prevails. Moreover, some uraniferous parts exist at the boundaries between the rock units.

Declaration of Competing Interest

None declared.

References

Abd El-Nabi, S.H., 1990. Geophysical Investigation of Aerospectrometric and Aeromagnetic Anomalies in the Vicinity of Gabel Idid El- Gedan Area, Eastern Desert, Egypt. Ph.D. Thesis. Faculty of Science, Ain Shams University, p. 159.

Abd El-Wahed, M.A., 2008. Thrusting and transpressional shearing in the Pan-African nappe southwest El-Sibai core complex, central Eastern Desert, Egypt. J. Afr. Earth Sci. 50, 16–36.

Aboelkhair, H., Saleh, G.M., Selim, E., Mogahed, A.N., 2020. Using airborne gamma-ray spectrometry for mapping radioactive zones in G. Kadabora area, central Eastern Desert,Egypt. Int. J. Mining Sci. (IJMS) 6, 1–10.

Aero-Service, 1984. Final Operational Report of Airborne Magnetic/radiation Survey in the Eastern Desert, Egypt. For the Egyptian General Petroleum Corporation (EGPC) and the Egyptian Geological Survey and Mining Authority (EGSMA). Aero-Service Division. Six Volumes, Houston (Texas, USA).

Ammar, A.A., Meleik, M.L., Fouad, K.M., 1983. Tectonic analysis of a sample area, Central Eastern Desert, Egypt, applying aeroradiometric and aeromagnetic survey data. Bull. Fac.

Earth. Sci., King Abdulaziz Univ., Jeddah, Kingdom of Saudi Arabia 6, 459–482.
Bennett, J.D., Mosley, P.N., 1987. Tiered tectonics and evolution, Eastern Desert and sinia, Egypt. In: Matheis, G., Schandelmeier, H. (Eds.), Current Research in African Earth Sciences. Balkema, Rotterdam, pp. 79–82.
Bregar, M., Bauernhofer, A., Pelz, K., Kloetzli, U., Fritz, H., Neumayr, P., 2002. A late Neoproterozoic magmatic core complex in the Eastern Desert of Egypt: emplacement of granitoids in a wrench-tectonic setting. Precambrian Res. 118, 59–82.
Chaturvedi, A.K., Lotter, C., Tripathi, S., Maurya, A.K., Patra, I., Parihar, P.S., 2013. Integrated application of heliborne and ground electromagnetic surveys for mapping EM conductor for uranium exploration and its subsurface validation, North Delhi Fold Belt, Rajasthan, India: a case study. Geophysics 78. B13–B24.
Conoco, 1987. Geological Map of Egypt, Scale (1:500,000), NG36 NE-Quseir Sheet and NG 36 SE-Gebel Hamata Sheet.
Darnely, A.G., Ford, K.L., 1989. Regional Airborne Gamma-Ray Surveys A review. In: Garland, G.D. (Ed.), Proceedings of Exploration, 87; Third Decennial International Conference on Geophysical and Geochemical Exploration for Minerals and Groundwater, vol. 3, pp. 229–240. Ontario, Canada, Geol. Sur., of Canada, Special.
Darnley, A.G., 1973. Airborne gamma-ray survey techniques, present and future. In: Uranium Exploration Methods – Proceedings of a Panel. International Atomic Energy Agency, Vienna (Austria), pp. 67–108 (320 pp).
Diab, H., Gabr, S.S., Abdel Fattah, T.A., Youssef, M.A.S., Khalil, I.K., 2022. Delineation of the subsurface boundary between the central and southern Eastern Desert, Egypt. Egypt. J. Remote Sens. Space Sci. 25, 903–918.
EGSMA (Egyptian Geological Survey and Mining Authority), 1992. Geological Map of Al Quseir Quadrangle, Egypt, Scale 1: 250000. Geo Surv Egypt, Cairo, Egypt.
El-Gaby, S., List, F.K., Tehrant, R., 1988. Geology, evolution and metallogenesis of the Pan-African belt in Egypt. In: El-Gaby, S., RO, Greiling (Eds.), The Pan-African Belt of Northeast Africa and Adjacent Areas. Viewing, Egypt. pp. 17–70
El Qassas, R.A.Y., Salaheldin, M., Assran, S.M.A., Abdel Fattah, T.A., Rashed, M.A., 2020. Airborne gamma-ray spectrometric data interpretation on Wadi Queih and Wadi Safaga area, central Eastern Desert, Egypt. NRIAG J. Astron. Geophys. 9, 155–167.
El-Rakaiby, M.L., 1988. The tectonic lineaments of the basement belt of the Eastern Desert, Egypt. Egypt. J. Geol. 32 (1–2), 77–95.
El-Ramly, M.F., 1972. A new geological map for the basement rocks in the eastern and south-eastern deserts of Egypt, scale 1:1,000,000. Ann. Geol. Surv. Egypt 2, 1–11.
EMRA (Egyptian Mineral Resources Authority), 2009. Geology of Wadi Al Barramiyah Quadrangle. Egypt.
Gaafar, I.M., 2014. Geophysical mapping, geochemical evidence and mineralogy for Nuweibi rare metal Albite granite, Eastern Desert, Egypt. Open J. Geol. 4, 108–136.
Gabr, S.S., Diab, H., Abdel Fattah, T.A., Sadek, M.F., Khalil, I.K., Youssef, M.A.S., 2022. Aeromagnetic and Landsat-8 data interpretation for structural and hydrothermal alteration mapping along the Central and Southern Eastern Desert boundary. Egypt. Egypt. J. Remote Sensing Space Sci 25, 11–20.
Garson, M., Krs, M., 1976. Geophysical and geological evidence of the relationship of Red Sea transverse tectonics to ancient fractures. Geol. Soc. Am. Bull. 87, 169–181.
Hamimi, Z., Zoheir, B.A., Younis, M.H., 2015. Polyphase deformation history of the Eastern Desert tectonic terrane in northeastern Africa. In: XII International Conference 'new Ideas in Earth Sciences'. Muscow, April 2015 (Abstract).
IAEA (International Atomic Energy Agency), 1988. Geochemical exploration for uranium. In: IAEA Technical Report Series No. 284. Vienna (Austria), p. 97.
Johnson, P.R., Andresen, A., Collins, A.S., Fowler, A.R., Fritz, H., Ghebreab, W., et al., 2011. Late Cryogenian-Ediacaran history of the Arabian–Nubian Shield: a review of depositional, plutonic, structural, and tectonic events in the closing stages of the northern East African Orogen. J. Afr. Earth Sci. 61, 167–232.
Mohanty, W.K., Mandal, A., Sharma, S.P., Gupta, S., Misra, S., 2011. Integrated geological and geophysical studies for delineation of chromite deposits: a case study from Tangarparha, Orissa, India. Geophysics 76, B173–B185.
Nikolakopoulos, K.G., Kamaratakis, E.K., Chrysoulakis, N., 2006. SRTM vs ASTER elevation products. Comparison for two regions in crete, Greece. Int. J. Rem. Sens. 27 (21). ISSN 0143-1161.
Pareta, K., Pareta, U., 2012. Quantitative Morphometric Analysis of a Watershed: Based on Digital Terrain Model and GIS. LAP Lambert Academic Publishing, Germany, pp. 1–93.
Patra, I., Chaturvedi, A.K., Srivastava, P.K., Ramayya, M.S., 2013. Integrated interpretation of satellite imagery, aeromagnetic, aeroradiometric and ground exploration data sets to delineate favorable target zones for unconformity related uranium mineralization, Khariar Basin, Central India. J. Geol. Soc. India 81, 299–308.
Sadek, M.F., Ali-Bik, M.W., Hassan, S.M., 2015. Late Neoproterozoic basement rocks of Kadabora suwayqat area, central Eastern Desert, Egypt: geochemical and remote sensing characterization. Arab. J. Geosci. 8, 1–21.
Saunders, D.F., Potts, M.J., 1976. Interpretation and application of high sensitivity airborne gamma-ray spectrometer data. In: Proceedings of the IAEA Symposium on Exploration for Uranium Ore Deposits. IAEA-SM 208/45, Vienna, Austria, pp. 107–125.
Soliman, N.M., Bayoumi, M.B., Salem, S.M., 2021. Mapping the alteration zones for uranium exploration in gabal Abu garadi area central Eastern Desert, Egypt, using Aster data. Earth Sci. 10, 36–48.
Stern, R.J., 2017. Neoproterozoic formation and evolution of Eastern Desert continental crust—the importance of the infrastructure-superstructure transition. J. Afr. Earth Sci. 146, 15–27.
Stern, R.J., Hedge, C.E., 1985. Geochronology and isotopic constraints on late Precambrian crustal evolution in the Eastern Desert of Egypt. Am. J. Sci. 285, 97–127.